Research Paper

Unraveling compacted graphite evolution during solidification of cast iron using in-situ synchrotron X-ray tomography

Chaoling Xu [a, *], Tim Wigger [b, c], Mohammed A. Azeem [b, d, **], Tito Andriollo [a], Søren Fæster [e], Samuel J. Clark [b, f], Zhixuan Gong [b, c], Robert Atwood [g], Jean-Claude Grivel [h], Jesper H. Hattel [a], Peter D. Lee [b, c], Niels S. Tiedje [a, ***]

[a] Department of Mechanical Engineering, Technical University of Denmark, 2800, Kgs. Lyngby, Denmark
[b] Mechanical Engineering, University College London, London, WC1E7JE, UK
[c] Research Complex at Harwell, Harwell Campus, Didcot, OX110FA, UK
[d] School of Engineering, University of Leicester, Leicester, LE17RH, UK
[e] Department of Wind Energy, Technical University of Denmark, 4000, Roskilde, Denmark
[f] Argonne National Laboratories, Lemont, IL, 60439, USA
[g] Diamond Light Source Ltd, Harwell Campus, Didcot, OX110DE, UK
[h] Department of Energy Conversion and Storage, Technical University of Denmark, 2800, Kgs. Lyngby, Denmark

ARTICLE INFO

ABSTRACT

In spite of many years of research, the physical phenomena leading to the evolution of compacted graphite (CG) during solidification is still not fully understood. In particular, it is unknown how highly branched CG aggregates form and evolve in the semi-solid, and how local microstructural variations at micrometer length scale affect this growth process. We present here the first time-resolved synchrotron tomography combined with a bespoke high-temperature environmental cell that allows direct observation of the evolution of CG and relates this dynamic process to the local surrounding microstructures in a cast iron sample during repeated melting and solidification. Distinct processes are identified for the formation of CG involving the nucleation, growth, development of branches and interconnection of graphite particles, ultimately evolving into highly branched graphite aggregates with large sizes and low sphericities. CG is found to nucleate with a spheroidal or a plate-like shape, developing branches induced by high carbon concentration, e.g. thin melt channels. Additionally, CG grows much faster than spheroidal graphite during subsequent cooling in solid state. The direct visualization of the dynamic solidification process provides unprecedented new insights into formation mechanisms of CG and correlating factors such as local microstructural variations, and guides the development of CG iron solidification models.

1. Introduction

Compacted graphite (CG) iron has been known more than 50 years ago, and is widely used in the automotive industry. As an engineering material it provides an outstanding combination of mechanical and thermal properties [1—3], i.e. good thermal conductivity and good vibration damping capacity. Previous studies with laboratory X-ray computed tomography (CT) [4], deep etching and focused ion beam nano-tomography [5] revealed that CG has a highly branched and interconnected aggregate morphology, which makes it difficult to locate the nucleation sites. While the size and morphology of graphite in CG iron play a key role in determining its properties [3,6,7], the evolution process of CG during solidification is still not fully understood. There are several aspects of growth of CG which are investigated by *ex situ* interrupted solidification techniques and post-solidification characterization, such as scanning electron microscopy (SEM) [8,9]. It is often reported that initial CG nucleates in a spheroidal shape, which degenerates/generates tails upon further cooling, grows in contact with the melt and

* Corresponding author.
** Corresponding author. School of Engineering, University of Leicester, Leicester, LE17RH, UK.
*** Corresponding author.
E-mail addresses: chaoxu@mek.dtu.dk, chlingxu@gmail.com (C. Xu), mohammed.azeem@leicester.ac.uk (M.A. Azeem), nsti@mek.dtu.dk (N.S. Tiedje).

branches further, developing into CG [10–12]. This degeneration and branching of graphite occur by twin boundary defects [10,13]. Furthermore, CG precipitating directly from an oxide and a sulfide was also detected by metallographic examination [14]. Recently, the morphology of CG obtained at different solidification stages was characterized using laboratory X-ray tomography (CT). It was found that CG evolves from spheroidal to cluster-like graphite, and then interconnects with each other, resulting in large CG clusters [15].

Graphite growth is determined by the diffusivity of carbon atoms at the interfaces between the solidified graphite and the melt phase [16], and therefore the local variations at these interfaces must be considered. Previous detailed X-ray analysis on melted cast iron demonstrated that undissolved graphite or carbon-rich clusters [17] exist and diffuse in the melt. Furthermore, the dynamic segregation of elements in the front of the solidification interface is a crucial aspect of solidification [18], especially the carbon segregation in terms of the graphite formation [17,19,20]. Understanding the nucleation and growth processes of graphite during the course of solidification thus requires in depth dynamic time-resolved data at local scale.

Experimentally, such dynamic data has been obtained only for very thin samples (<200 μm) by two-dimensional (2D) radiography [21,22]. However, such experiments have the inherent limitation that the confined 2D geometry is not representative of the conditions under which the solidification of a component takes place in 3D, and the actual sizes and shapes of graphite particles cannot be determined. Alternatively, static and statistical data have been obtained from a series of interrupted solidification experiments [10,15] and combined with simulations to estimate the cooling curves and thus to investigate the melt preparation before casting [23]. However, such approach does not capture the effects of local microstructural variations. Consequently, despite the substantial efforts devoted to the understanding towards the formation of CG, limited fundamental knowledge about the evolution of CG has been obtained, highlighting the need to observe the solidification directly in the sample bulk. Two experiments on the formation of graphite during solidification have recently been performed using time-resolved synchrotron X-ray CT [24,25]. However, in one case the temporal resolution was insufficient to allow mapping of the dynamic evolution of CG [24], and in the other the spatial resolution is not sufficient to image microstructural variations [25].

In the present work, we use an upgraded synchrotron X-ray CT setup combined with a bespoke high-temperature environmental cell [25] that allows us to surmount these challenges such that we can directly observe the nucleation, growth and branching processes of CG during solidification, and resolve local instantaneous microstructural variations around the graphite. We present results of an experiment where we first repeatedly melted and cooled a ductile cast iron sample in a controlled manner to allow the formation of CG. In the cooling stage of the last cycle, a series of back-to-back X-ray tomograms were acquired over time. Accordingly, we captured how the highly branched CG aggregate forms in the semi-solid phase, and how local microstructural variations affect the evolving process.

2. Methods

The initial composition of the material is shown in Table 1, which is the same as in our previous investigation [25]. A master alloy was prepared by melting 15 kg of cast iron in a graphite crucible, followed by addition of a standard Mg treatment alloy, immediately before the alloy was cast into 500 g ingots. From these ingots samples of 12 mm in length and 2 mm in diameter were machined.

Table 1
Initial chemical composition in wt.% of selected elements in the sample and eutectic temperature of the stable system.

C	Si	Mg	Mn	P	S	Ce	La	T^{eut}
3.6	1.9	0.08	0.1	0.02	0.001	0.01	0.01	1162 (°C)

The amount of Mg in the cast iron melt was controlled to ensure spheroidal growth in the first several solidification cycles. Synchrotron X-ray absorption-contrast CT was performed at the beamline I12 [26], Diamond Light Source, UK. A high-temperature environmental cell was used for *in-situ* X-ray CT, designed for solidifying materials with a melt point exceeding 1300 °C, controlled cooling rates as slow as 10^{-2} °C/s (K/s) and a temperature precision of ±0.5 °C. A vertical section view of the cell and a schematic of the sample module are provided in Fig. 1a and b, respectively. The sample with a size of Φ2 × 12 mm was encapsulated in a Φ2.1 mm argon filled quartz tube, and supported by a quartz rod at the bottom to prevent it from moving during the course of solidification. The encapsulated sample was mounted on an alumina rod connected to a rotation stage, enabling rotation for tomography. Temperature was measured with an R-type thermocouple located outside the casting by 3 mm away from the sample surface.

The sample was repeatedly heated and cooled as shown in Fig. 1c. In each cycle, the sample was heated to 1178 °C, briefly held to ensure the material melted within the whole gauge volume, and then cooled at a rate of 0.3 °C/s to 1000 °C. The present analysis is based on the last cooling cycle, which is marked as green in Fig. 1c. During the time-resolved high-temperature solidification experiment, a monochromatic beam with an energy of 60.9 keV and a PCO edge camera with a pixel size of 3.24 μm were used for tomographic imaging. In total, 200 tomograms with a size of $2981 \times 3013 \times 3434$ μm³ were acquired, each of which consists of 720 projections over 180° with an exposure time of 5 ms and a frame rate of 182 Hz (or 4 s per tomogram). Image reconstruction and registration were performed using SAVU® [27] and Avizo® respectively. The post processing and segmentation of data were performed using MATLAB®. A sub-volume with a size of $1040 \times 878 \times 910$ μm³ was extracted to perform statistical analysis. Particles with a size smaller than 8 voxels were excluded in our statistical analysis to eliminate the effect of noise. The smallest graphite particles included in the analysis is thus with a diameter of 7.8 μm.

Finally, the graphite morphology of the entire sample was characterized after solidification at room temperature using laboratory X-ray CT with a resolution of $1.1 \times 1.1 \times 1.1$ μm³ and SEM with accelerating voltage of 15 kV and an emission current of 2.32 A.

3. Results and discussion

Considering SEM sections of the whole specimen after the experiment (Fig. 2a–d), shrinkage formed during melting and solidification is clearly visible along with some porosities at the top of the sample. Based on the morphology of graphite, the sample volume can be divided into two regions: Region 1 with only lamellar graphite (LG) and a thickness of 1–3 μm (see Fig. 2b and c), and region 2 with a mixture of spheroidal graphite (SG) and CG (see Fig. 2b and d). The size of SG varies from a few micrometers to about 40 μm in diameter. It should be noted that the small SG generally has a relatively high sphericity, while the SG with a large size tends to take more irregular forms. The CG is curved, elongated, branched and randomly oriented.

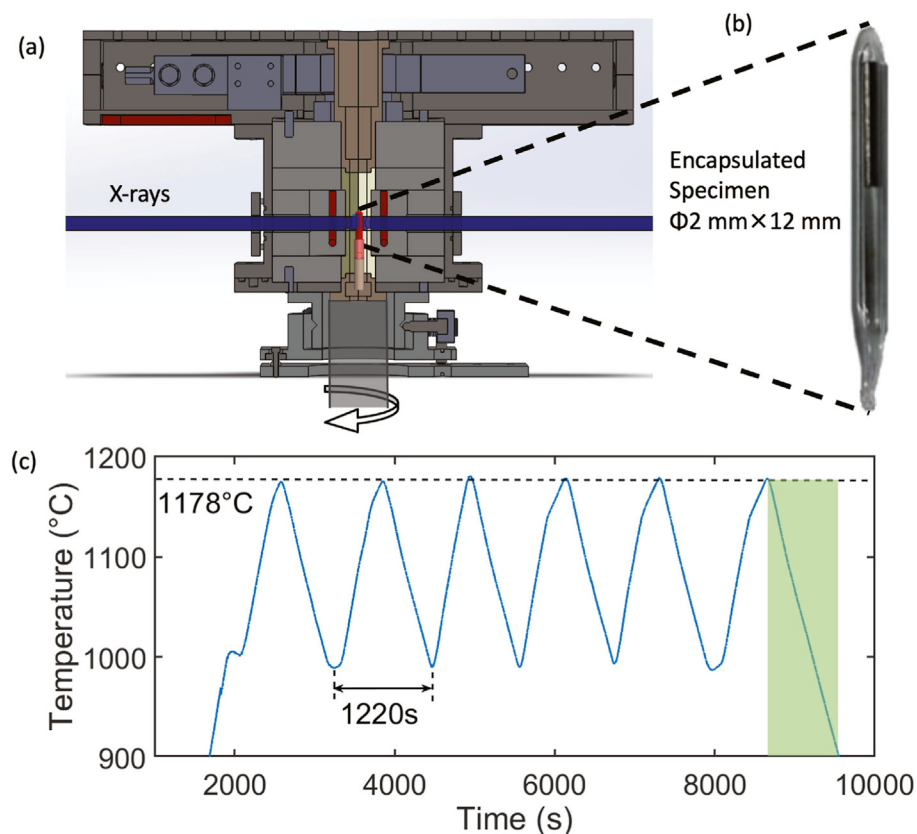The branch thickness is in the range of 2–20 μm. The resulting

Fig. 1. (a) Schematic of the environmental cell setup at the I12 beamline of Diamond Light Source, (b) quartz encapsulated sample and (c) heating and cooling program. The dashed line in (c) shows the highest temperature during the thermal cycling process, and the cooling stage in the last cycle is marked as green. (A colour version of this figure can be viewed online.)

mixture of graphite morphologies is in agreement with that of other re-melting experiments [28]. The statistical analysis in this paper was conducted using a central part of the volume with a size of $880 \times 910 \times 1040$ μm^3, within which predominantly SG and CG morphologies are observed (see the light green frame in Fig. 2a), to focus on the nucleation and growth of the CG.

3.1. Nucleation

The first graphite particle in the analyzed volume is detected at 1129 °C with a relatively large size, presumably floating up from a lower region with a lower temperature due to buoyancy forces. Afterwards, several graphite embryos are observed in the temperature range of 1129 °C–1117 °C. During the following period, the nucleation rate dramatically increases and thousands of graphite particles form at temperatures between 1117 °C and 1099 °C. A subset of the analyzed volume is shown in Fig. 2e–k. Most graphite embryos are in a spheroidal shape and a few in plate-like shapes (Fig. 2e). With decreasing temperature, more particles nucleate whilst those formed earlier develop into larger sizes simultaneously. One of the most remarkable observations from the *in-situ* examination is that the plate-like CG grows very fast compared to SG, and develops into a highly branched aggregate structure, resulting in the CG particles as the dominating morphology in the volume. Although most spheroidal embryos are observed to keep their spheroidal shapes during their growth, it is interesting to note that several spheroidal embryos develop protrusions as seen from the blue graphite in Fig. 2e and f.

Furthermore, the *in-situ* CT characterization allows to track the morphology of all graphite particles by detecting the initial embryo

of each graphite particle. It is evident that almost all particles are initially detected with a sphericity larger than 0.75. However, 87% of these have a sphericity larger than 0.9 and about 6% are smaller than 0.85. For example, two green particles marked with arrows in Fig. 2e have a sphericity of 0.77 and 0.86 showing a plate-like structure instead of a spheroidal shape. These findings are consistent with previous research through quenching experiments [10–12,14], which stated that CG may form not only with a mainly spheroidal shape, followed by growing into tadpole graphite and developing into CG, but also with CG growing directly on the nuclei. It should be noted that the plate-like embryos might form with a spheroidal shape and a size smaller than the spatial resolution in present study, and then grow into a larger plate-like graphite.

Due to low X-ray attenuation contrast between the austenite and the liquid phase at high temperatures, precisely segmenting austenite from the liquid phase was not possible. Nevertheless, variations in the attenuation are clearly evident in 2D sections of the tomograms, as a result of the difference in density between the austenite and liquid. Some of these 2D sections showing changes in the microstructure as a function of decreasing temperatures are visualized in Fig. 3a–g, with low attenuation in blue (graphite, liquid) and high attenuation in red (solid). As temperature decreases and solidification progresses, graphite particles nucleate and grow in the melt (see Fig. 3a), rejecting the Fe atoms at the solidifying front and increasing the Fe content in vicinity. Subsequently, austenite nucleates and grows as the temperature decreases further (Fig. 3b) at sites close to the graphite particles and along the ligaments between nodules, partially or fully encapsulating the graphite particles. Austenite shells develop at the liquid-graphite interfaces, significantly reducing the flux of carbon atoms
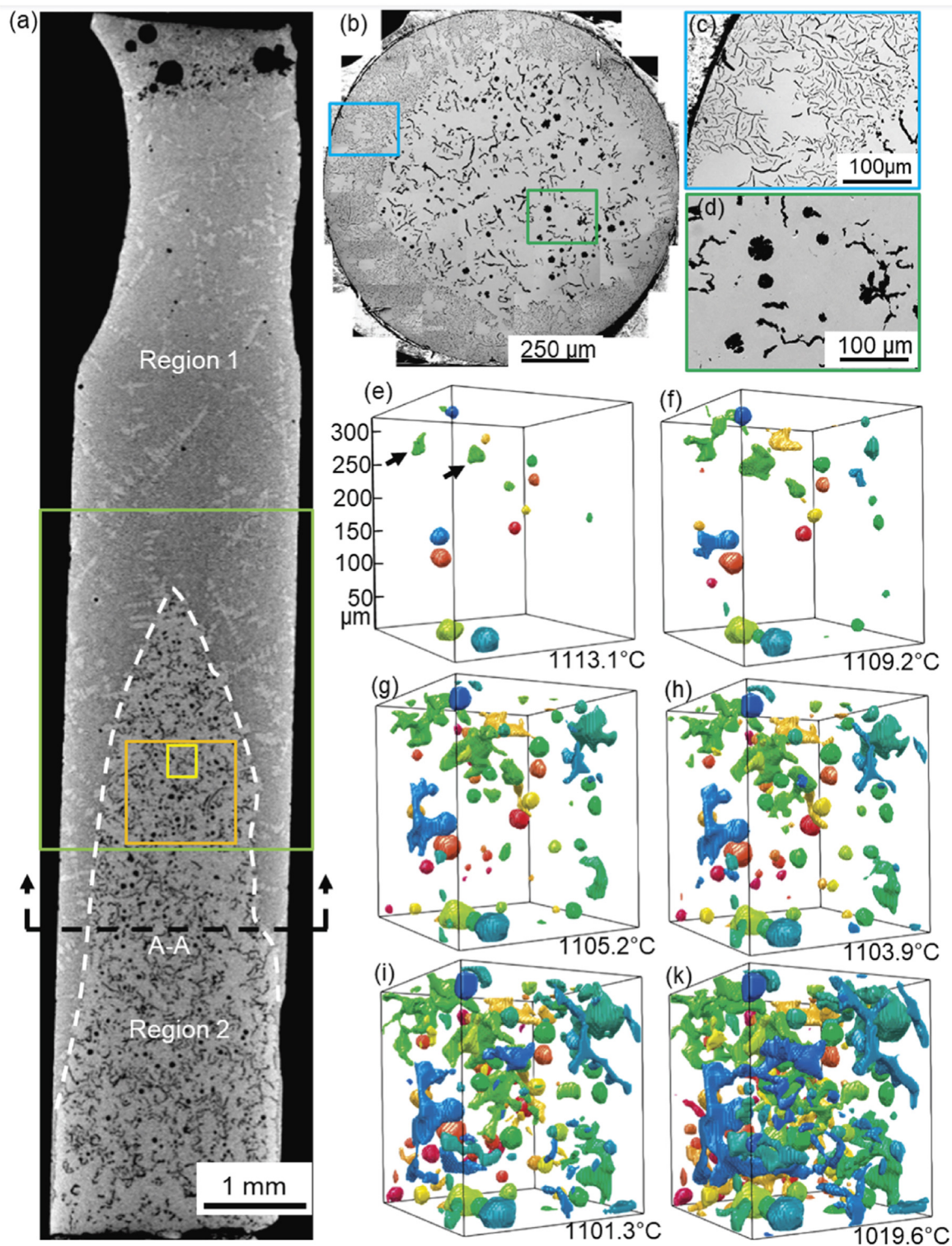
Fig. 2. (a) A 2D slice extracted from laboratory X-ray CT scans revealing the post-solidification graphite morphologies in the entire 12 mm sample at room temperature. The white dashed line divides the volume into two regions: region 1 with only lamellar graphite and region 2 with a mixture of spheroidal and compacted graphite. The region characterized by synchrotron X-ray is marked with a light green frame. The microstructures on the A-A cross section is shown in (b), a montage of SEM images. The local microstructures in the blue and green rectangles in (b) are shown in (c) and (d) respectively at high magnifications, where flaky, compacted and spheroidal graphite particles can be seen clearly. The region of the sample in which time-resolved observations were performed using synchrotron X-ray is highlighted by a light green rectangle in (a). Orange in (a) highlights a central sub-volume where only spheroidal and compacted graphite particles were observed, and the statistics in the present paper are from the central sub-volume. The evolution of graphite particles in a part of the sub-volume, marked as yellow in (a), is shown in 3D in (e)–(f). The color in (e)–(f) is randomly selected to show individual particles and does not have any other specific meaning. (A colour version of this figure can be viewed online.)
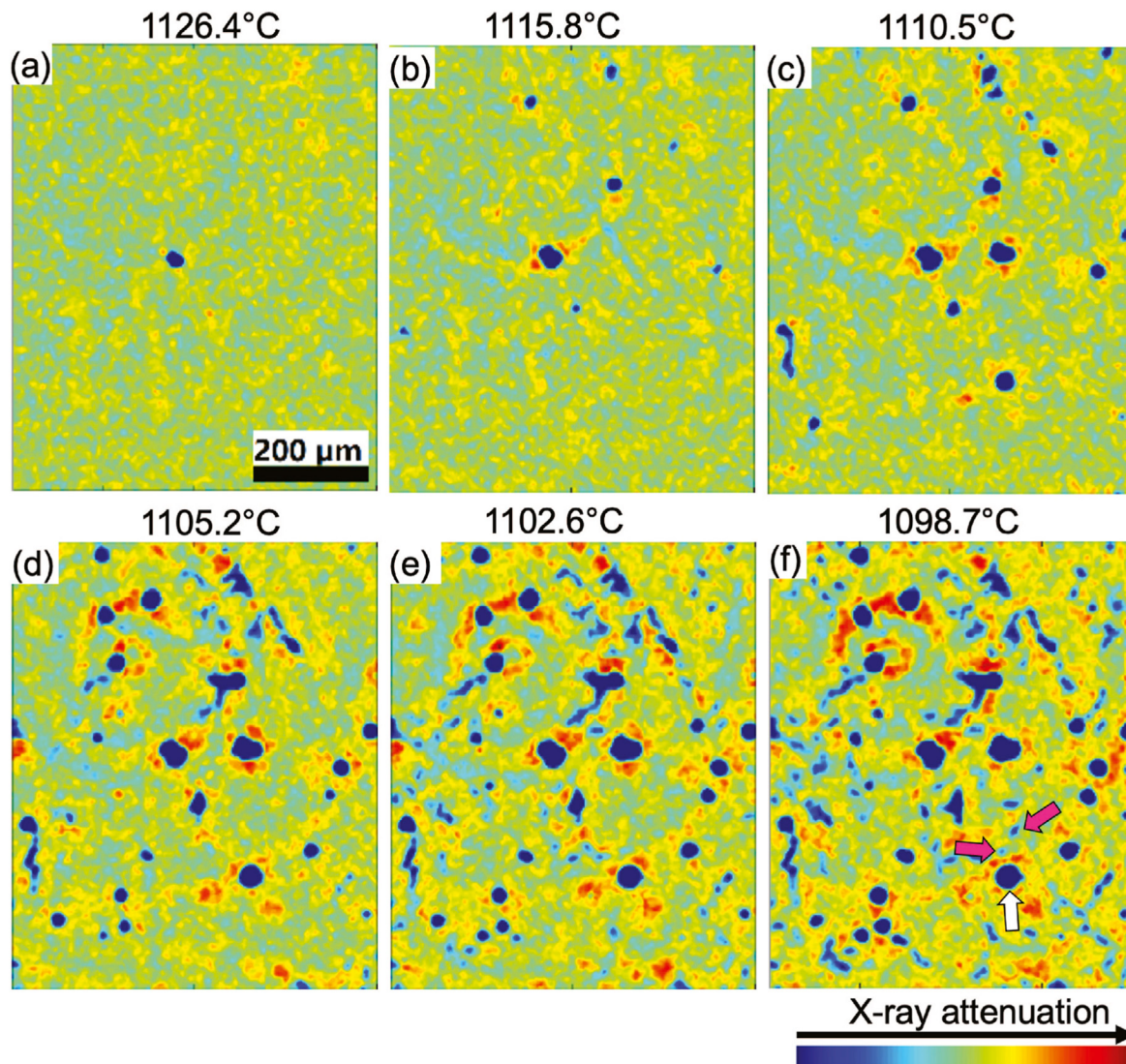
Fig. 3. (a)–(f) 2D slices extracted from *in-situ* synchrotron tomography revealing nucleation of graphite particles and engulfment by austenite during the course of solidification. The color represents the X-ray attenuation, which increases from blue to red. The dark blue spots and bright red regions are thus considered as graphite particles and austenite respectively. One white and two pink arrows mark one primary and two secondary graphite particles respectively. (A colour version of this figure can be viewed online.)

and growth of graphite. The carbon atoms concentrate at the solidification front of the austenite again, enabling secondary nucleation of graphite in the melt near the austenite. Fig. 3 shows that secondary nucleation accelerates once the primary graphite is engulfed by the austenite, especially the nucleation of CG. One example is shown in Fig. 3f, where two graphite embryos (marked with pink arrows) form immediately after a primary graphite (marked using a white arrow) is encapsulated. This observation is in good agreement with earlier studies by in-situ synchrotron radiography and tomography [20], which reported that the engulfment of graphite particles into austenite in a short duration promotes the secondary nucleation of graphite particles.

The *in-situ* examination allows to investigate the variation in size versus temperature. By extrapolating each graphite particle's growth back to zero radius, the highest temperature at which nucleation of the graphite particles occurred is estimated as the nucleation temperature. Fig. 4a and b with y axis in linear and log scale respectively are histograms of the nucleation temperature of all tracked graphite. It shows that the number of graphite particles increases until a temperature of about 1104 °C is reached, after

which it decreases again. No graphite particles form below 1090 °C (Fig. 4b), indicative of the end of solidification. This reveals that nucleation is active throughout the interval of graphite precipitation but apparently with varying nucleation rate.

Interestingly, the majority of primary graphite nucleating in the early stage and more than half of the graphite forming in the last stage are found to be SG at the end of solidification (Fig. 4a). Most secondary graphite forming in the intermediate stage, however, is observed to develop into CG. This result confirms previous findings by colored etching, stating that SG can form either in the first or in the last solidified region [29]. In the beginning of solidification, more SG nucleates as a result of relatively high Mg in the melt, followed by formation of CG caused by the consumption of Mg atoms. The solidifying eutectic rejects Mg, enriching Mg in the remaining melt and promoting SG formation [29,30].

Moreover, it can be noticed in Fig. 4b that the nucleation frequency curve of SG is bimodal, which corresponding to the primary and second nucleation of graphite particles. SG forms earlier tend to have a larger size due to the longer growth time [31].The result is thus in line with previous results on the final size distribution of
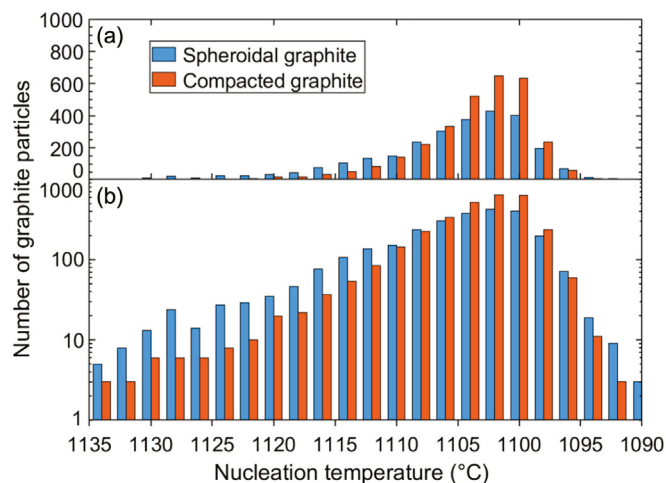
Fig. 4. (a) Histogram with y asix in linear scale and (b) with y axisin log scale of nucleation temperature which is defined as highest temperature at which nucleation of the graphite particles occurred. The graphite particles nucleating in the early stage are found to be SG at the end of solidification, while graphite embryos forming in the intermediate stage are observed to develop into CG. (A colour version of this figure can be viewed online.)

graphite particles [32]. The nucleation curve of CG is monotonic when compared to the bimodal curve of SG. It might be caused by the much lower nucleation rate of CG in the beginning of solidification.

3.2. The evolution of global size and morphology

Once the carbon clusters reach a critical radius forming the graphite embryos, they will spontaneously grow. The temporal resolution of the present time-resolved characterization allows determination of how the morphology of graphite evolves exactly during the course of solidification, i.e. quantification of size and sphericity at different solidification stages, by comparing the microstructures at each temperature interval. The number of graphite particles is plotted as a function of temperature for different size categories in Fig. 5a. It can be seen that the size distribution is increasingly dominated by the smallest particle sizes until 1100 °C where the nucleation seems to have ceased or slowed down (see Fig. 4). Below 1100 °C the graphite continues growing, hence decreasing the number of small graphite particles. As mentioned above, most graphite nucleates with a sphericity larger than 0.9, thus the shape distribution is dominated by spheroidal particles as shown in Fig. 5b. As the graphite nucleation ceases before 1090 °C, only graphite growth occurs thereafter and it is thus reasonable to assume that the reductions in sphericity after 1090 °C are primarily due to graphite growth. This is substantiated by the clear tendency for the graphite with a low sphericity to have larger volumes than those with a high sphericity after solidification, as is shown in Fig. 6a.

The *in-situ* tomography data also allows tracking from which nucleus each individual final graphite particle develops, and thus determining the change in sphericity. The sphericity difference between the first nucleus and the corresponding fully grown graphite particle at the end of solidification is calculated for all particles, and the distribution is shown in Fig. 6b. The majority of embryos develop into graphite particles with a lower sphericity, while 9% of the embryos retain their high sphericity during growth.
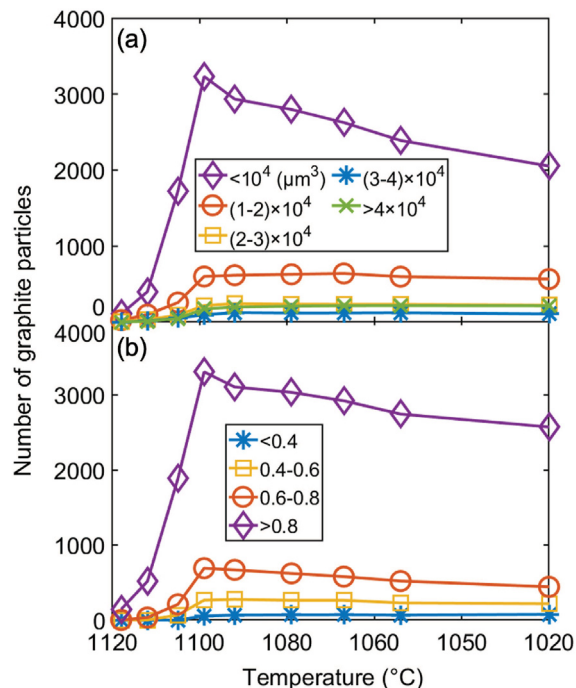

Fig. 5. (a) Volume size distribution as a function of temperature at different size categories, and (b) sphericity distribution as a function of temperature at different sphericity groups. The morphology of graphite is dominated by the smallest particle sizes and the highest sphericity. (A colour version of this figure can be viewed online.)

3.3. Growth of SG

The above analysis provides to a global understanding of the morphology development, which is visualized in Fig. 2e−k and statistically analyzed in Fig. 5. It is found that large graphite particles with a sphericity lower than 0.6, identified as CG in the analyzed volume, are initially observed with a mainly spheroidal shape and a few in a plate-like shape, then grow into a highly branched aggregate. To understand why the morphology evolves in this pattern and to relate this general observation to individual growth of both SG and CG, selected particles are monitored over time (Fig. 7). The data shows that the SG particles grow according to previously reported three stages [33,34]. Initially, the graphite grows with a large growth rate immediately after nucleation, caused by its uninhibited access to the carbon-rich liquid. Then austenite forms around the graphite, encapsulating the particles and detaching the graphite from a direct supply of carbon in the liquid. Next, the growth is controlled by diffusion of carbon through the austenite shell, leading to a lower and nearly constant growth rate. As the temperature approaches 1100 °C, the carbon supply from the liquid is nearly exhausted and a new growth stage is observed during the subsequent cooling. This is fully consistent with previous reports of divorced eutectic growth of graphite and austenite, and engulfment of graphite during solidification of ductile cast iron [35,36].

3.4. Growth, branching and interconnection of CG

Contrary to the growth of the SG, the growth curve of the CG can be divided into three different stages: Slow growth in a short period after nucleation, growth with a significantly high growth rate, and very slow growth in the solid cooling stage. The gradual growth in the third stage is clearly revealed by a linear fitting (see grey dashed lines in Fig. 7), though the volume of the graphite shows fluctuation
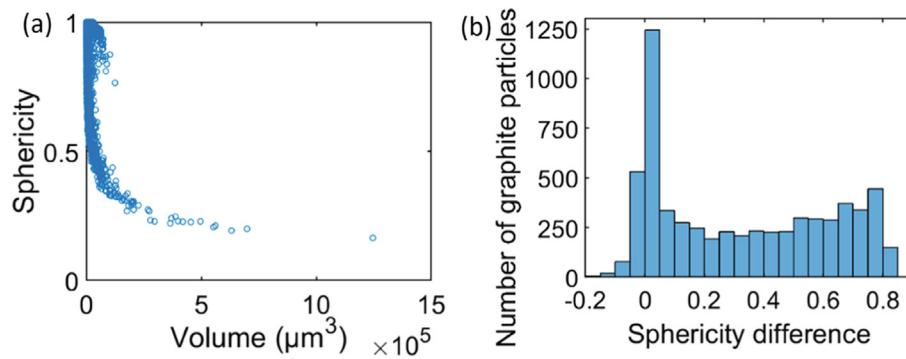
Fig. 6. (a) Correlation of sphericity and volume size at the end of solidification, and (b) histogram of sphericity difference between the initial graphite embryos and corresponding particles at the end of solidification. The graphite particles with a low sphericity tend to have larger volumes than those with a high sphericity after solidification. The majority of graphite embryos develop into particles with a lower sphericity. (A colour version of this figure can be viewed online.)
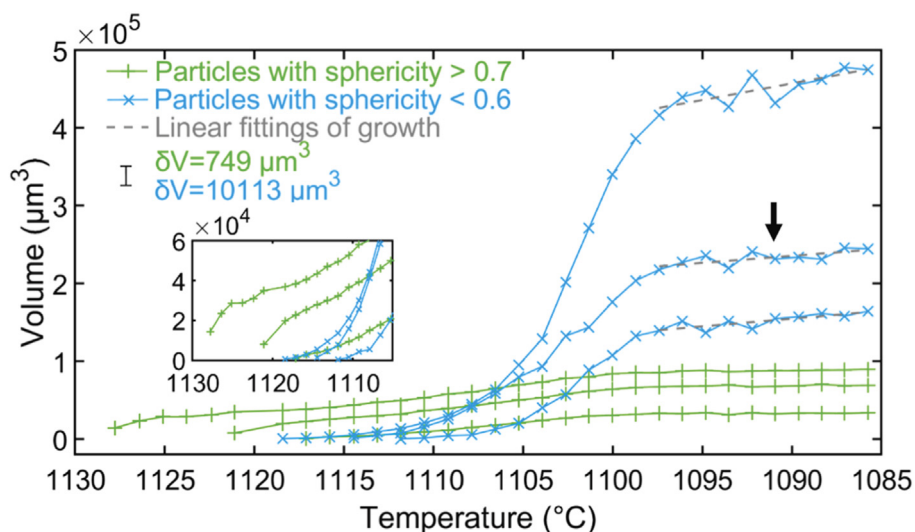

Fig. 7. Growth of six graphite particles during the course of solidification as a function of temperature: green and blue plots are for particles with sphericity larger than 0.7 and smaller than 0.6 respectively. The volume of each particle was approximated by a linear fitting using data from the temperature interval [1097 °C, 1086 °C] and shown as grey dashed lines, revealing the gradual growth of particles in the temperature interval. The errors on the volume (δV) of these two types of graphite are listed. The black arrow indicates the particle selected for discussing compacted graphite evolution, as detailed in in Fig. 8. The inset shows the initial growth of particles. (A colour version of this figure can be viewed online.)

due to segmentation variations. It has been widely reported that the CG has a worm-like structure in 2D and a highly branched aggregate structure in 3D, i.e. irregularly shaped plates with multiple nodule-like particles attached to it [4,11,33]. Previously, single nucleus has been detected in quasi-spheroidal CG aggregate by chemical composition characterization on a 2D section [15]. However, it is not clear if there are more nuclei located in other sections of the CG aggregate. Additionally it is inconceivable that one CG particle nucleates at one site and grows to form a particle with a size of 2 mm. CG particles as large as these would form by interconnection of several smaller particles, which has also been reported before [15].

It is thus of interest to use the available 4D data to unravel how such large CG structures form and to investigate the extremely high growth rate in the second stage. Fig. 8 shows the morphology evolution of the CG particles marked with an arrow in Fig. 7. For the first time we directly observe graphite nucleating at different sites and growing into larger sizes, followed by the development of branches and interconnections with each other. The present findings are well substantiated by previous 3D microstructure investigations on the morphology of CG [4,15]. By comparing the

growth curve in Fig. 4 and the morphologies in Fig. 8, it is clear that the steep increases in the growth rates are mainly a result of the interconnection of graphite particles.

The number of single particles that a final aggregate particle consists of can be calculated by tracking the whole evolution process. To further investigate the role of the particle interconnection in the formation of CG, a new parameter, connectivity, is defined here as *the number of single particles involved in the formation of a CG particle at the end of solidification*. Statistical analysis regarding the size distributions (in terms of volume) and the evolution process of CG has been conducted, and the result is shown in Fig. 9. The correlation between the size and the connectivity is estimated using a linear fit: $V = 7898 \times Conn - 848.7$, where V and $Conn$ are the volume size (μm^3) and connectivity of the CG respectively. As plotted using a dashed line in Fig. 9, it shows a clear positive linear relation. This is substantiated by the fact that a CG in millimeter scale could form with temperature decreasing from 1230 °C to 1139 °C within 2 min [15].

This absorption contrast due to X-ray attenuation can also be related to the carbon concentration in the melt. An example of the CG in Fig. 7 is shown in Fig. 10 as contour maps of a 2D section at
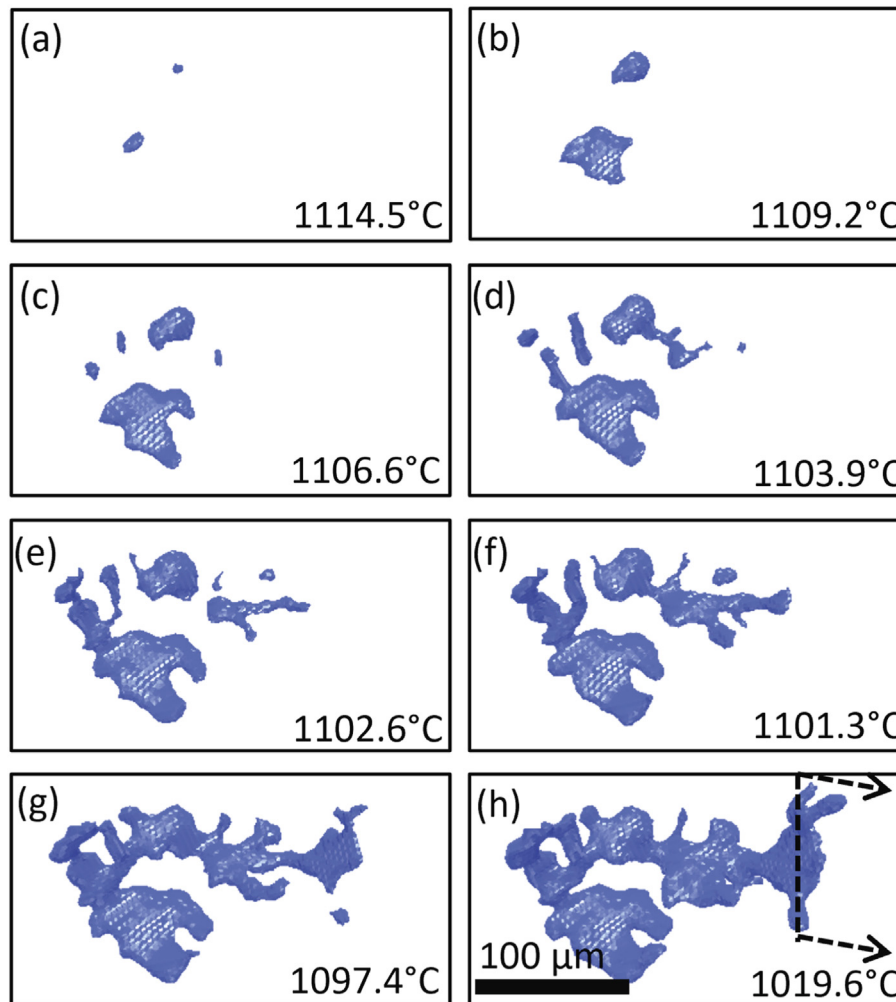
Fig. 8. Storyboard of the evolution of a compacted graphite particle showing nucleation, growth and interconnection. Graphite particles nucleate at different sites, grow into larger sizes, develop branches, and interconnect with each other. (A colour version of this figure can be viewed online.)
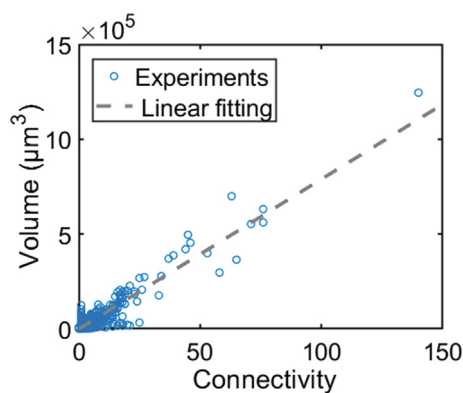

Fig. 9. vol size of graphite particles as a function of connectivity. The correlation is estimated by a linear fitting indicated with dashed lines, showing a clear positive linear relation between the volume size and the connectivity. (A colour version of this figure can be viewed online.)

different solidification stages. The graphite is shown in white, whilst the colors of the surrounding field reflect the attenuation. The yellow and red regions contain less carbon (an indication for austenite) and the dark blue regions are considered to be thin melt channels between the solid structures. It is observed that the SG grows isotropically as a result of the similar carbon content around the SG. Another SG nucleates at 1101 °C (Fig. 10c) and grows laterally toward high carbon concentration forming an elongated shape (Fig. 10d), a result of its direct contact with the melt. Another particle nucleates in the same carbon-rich region (Fig. 10e), then degenerates and becomes a protrusion (Fig. 10f). Remarkably, these two particles grow along the thin melt channel towards each other and interconnect forming one worm-like CG (Fig. 10g and h). This observation further strengthens the hypothesis that high carbon concentration, i.e. thin melt channels, induces the development of branches and interconnection of particles. The branching mechanism is believed to be a combination of twinning and rotation [10,13,37].

By comparing the last synchrotron tomogram at the end of solidification with the laboratory CT obtained after the experiments at room temperature, further continued growth of graphite particles during subsequent cooling and eutectoid transformation is analyzed. It is confirmed that all the highly branched CG aggregates grow and interconnect to a large CG structure during subsequent cooling in solid state, providing further evidence for the role played by interconnection of graphite particles in the formation process. However, it should be noted that the large CG might already form at the end of solidification by very fine graphite ligaments, which
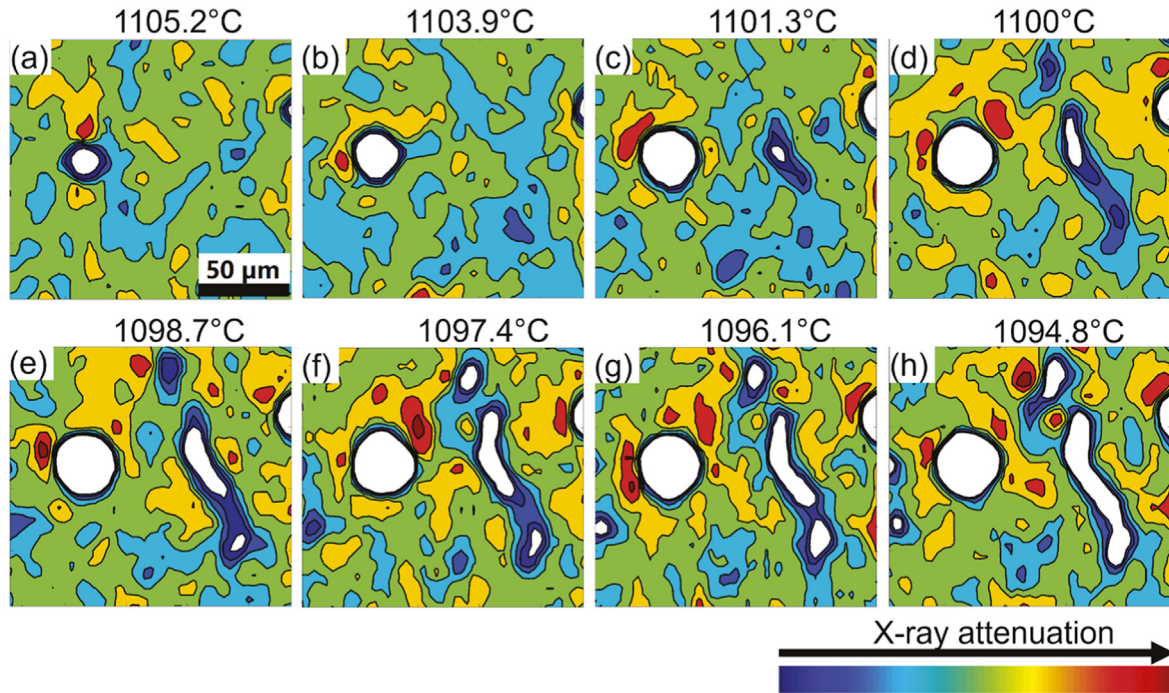
Fig. 10. Contour maps showing the evolution of graphite particles on a 2D section. The graphite particles are marked as white, while the color of other pixels represents the attenuation of X-ray as shown in the color legend. Growth and development of protrusion are induced by high carbon concentration. (A colour version of this figure can be viewed online.)

cannot be detected with the synchrotron CT. Furthermore, the phenomenon is observed in the tiny sample with a fixed cooling rate, which is different from large commercial casting. The graphite morphology at room temperature in the same volume as Fig. 2e—k is shown in Fig. 11, indicating that the large CG extends over the entire volume. The remaining graphite, which is not attached to the CG, is SG with degenerate features. The particle growth from the end of solidification to room temperature is between 5% and 26% with an average of 17%, relative to their size at the end of solidification, while the growth value for the CG is 44%. The diffusion distance of carbon atoms in the steel matrix around highly branched CG should be much shorter than that around SG, and it thus appears reasonable to observe more growth in CG.

4. Conclusion

The present work highlights the unique capability of synchrotron CT for direct observations of the evolution of CG during solidification. During repeated melting and solidifying of a ductile cast iron sample, it was discovered that: (i) CG graphite is detected initially in mainly spheroidal shapes but with few particles in plate-like shapes, (ii) except for initial growth and branching, interconnection of graphite particles plays a crucial role in the formation of CG, and (iii) CG grows much faster than SG during subsequent cooling in solid state. Furthermore, the growth and branching of the graphite appears to be induced by high carbon concentrations, *i.e.* thin melt channels between solid structures.
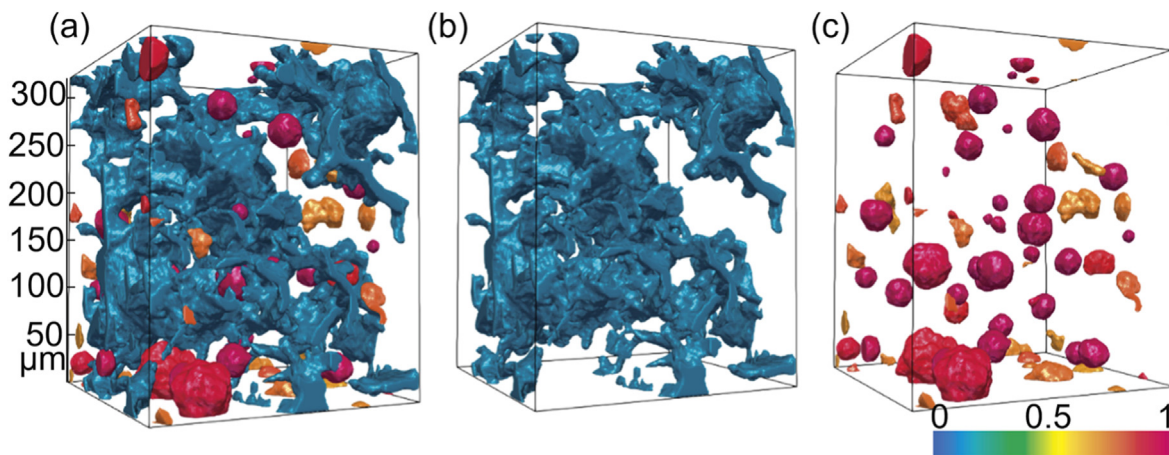

Fig. 11. Laboratory CT microstructures in the region same with Fig. 2e—k: (a) all particles in the volume, (b) the largest compacted graphite particle and (c) the rest graphite particles. The color represents the sphericity of graphite particles. Almost all CG particles forming during solidification grow further and interconnect with each other during the solid cooling process to form a huge highly branched CG aggregate. (A colour version of this figure can be viewed online.)

Our experiments demonstrate that the formation mechanisms of complex graphite structures can be observed directly. The next steps will be to investigate branching and interconnection of CG in more detail, such as the interaction between graphite and austenite dendrites during solidification. The ultimate goal for this type of investigation is to study the mechanisms controlling the evolution of graphite particles, to develop models for solidification and thus to facilitate targeted manufacturing processes for cast iron with desired microstructures.

CRediT authorship contribution statement

Chaoling Xu: Conceptualization, Investigation, Resources, Data curation, Formal analysis, Writing — original draft, Writing — review & editing, Visualization. **Tim Wigger:** Investigation, Data curation, Writing — review & editing. **Mohammed A. Azeem:** Conceptualization, Investigation, Resources, Writing — review & editing, Supervision, Funding acquisition. **Tito Andriollo:** Investigation, Writing — review & editing, Funding acquisition. **Søren Fæster:** Investigation, Writing — review & editing, Funding acquisition. **Samuel J. Clark:** Investigation, Writing — review & editing. **Zhixuan Gong:** Investigation, Writing — review & editing. **Robert Atwood:** Investigation, Writing — review & editing. **Jean-Claude Grivel:** Investigation, Writing — review & editing. **Jesper H. Hattel:** Funding acquisition, Project administration, Writing — review & editing. **Peter D. Lee:** Conceptualization, Investigation, Resources, Writing — review & editing, Supervision, Funding acquisition. **Niels S. Tiedje:** Conceptualization, Investigation, Resources, Writing — review & editing, Supervision, Funding acquisition.

Declaration of competing interest

The authors declare that they have no known competing financial interests or personal relationships that could have appeared to influence the work reported in this paper.

Acknowledgement

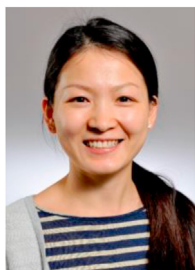## References

[1] S. Dawson, S. Limited, Castability, product design, and production of compacted graphite irons, in: D.M. Stefanescu (Ed.), ASM Handb., 2017, pp. 665—675, https://doi.org/10.31399/asm.hb.v01a.a0006328.

[2] S. Dawson, S. Limited, Specification, selection, and applications of compacted graphite irons, in: D.M. Stefanescu (Ed.), ASM Handb., 2017, pp. 659—664, https://doi.org/10.31399/asm.hb.v01a.a0006312.

[3] D.M. Stefanescu, Compacted graphite iron, in: D.M. Stefanescu (Ed.), ASM Handb., 1990, pp. 56—70, https://doi.org/10.31399/asm.hb.v01.a0001004.

[4] C. Chuang, D. Singh, P. Kenesei, J. Almer, J. Hryn, R. Huff, Application of X-ray computed tomography for the characterization of graphite morphology in compact-graphite iron, Mater. Char. 141 (2018) 442—449, https://doi.org/10.1016/j.matchar.2016.08.007.

[5] A. Velichko, C. Holzapfel, F. Mücklich, 3D characterization of graphite morphologies in cast iron, Adv. Eng. Mater. 9 (2007) 39—45, https://doi.org/10.1002/adem.200600175.

[6] J.M. Guilemany, N. Llorca-Isern, Relationships between microstructure and properties of unalloyed compacted graphite cast irons, Mater. Sci. Eng. 130 (1990) 241—246, https://doi.org/10.1016/0921-5093(90)90064-A.

[7] R.W. Gregorutti, J.E. Grau, Mechanical properties of compacted graphite cast iron with different microstructures, Int. J. Cast Met. Res. 27 (2014) 275—281, https://doi.org/10.1179/1743133614Y.0000000118.

[8] D.M. Stefanescu, Microstructure evolution during the liquid/solid transformation in cast iron, in: D.M. Stefanescu (Ed.), ASM Handb., 2017, pp. 59—80, https://doi.org/10.31399/asm.hb.v01a.a0006304.

[9] X. Den, P. Zhu, Q. Liu, Structure and formation of vermicular graphite, in: H. Fredriksson, M. Hillert (Eds.), Phys. Metall. Cast Iron, Third Int. Symp., 1984, pp. 141—150.

[10] G. Alonso, D.M. Stefanescu, P. Larrañaga, R. Suarez, Understanding compacted graphite iron solidification through interrupted solidification experiments, Int. J. Cast Met. Res. 29 (2016) 2—11, https://doi.org/10.1179/1743133615Y.0000000020.

[11] C. Chuang, D. Singh, P. Kenesei, J. Almer, H. Hryn, R. Huff, 3D quantitative analysis of graphite morphology in high strength cast iron by high-energy X-ray tomography, Scripta Mater. 106 (2015) 5—8, https://doi.org/10.1016/j.scriptamat.2015.03.017.

[12] J. Lacaze, D. Connétable, M.J. Castro-Román, Effects of impurities on graphite shape during solidification of spheroidal graphite cast ions, Materialia 8 (2019), https://doi.org/10.1016/j.mtla.2019.100471.

[13] J. Qing, V.L. Richards, D.C. Van Aken, Growth stages and hexagonal-rhombohedral structural arrangements in spheroidal graphite observed in ductile iron, Carbon N. Y. 116 (2017) 456—469, https://doi.org/10.1016/j.carbon.2017.01.063.

[14] G. Alonso, D.M. Stefanescu, P. Larrañaga, R. Suarez, Graphite nucleation in compacted graphite cast iron, Int. J. Met. 14 (2020) 1162—1171, https://doi.org/10.1007/s40962-020-00441-2.

[15] G.Q. Shi, Z. Yang, J.P. Li, D. Tao, Z.J. Ma, Investigation on the graphite nucleation and growth mechanism of the compacted graphite iron, J. Mater. Res. Technol. 9 (2020) 8186—8196, https://doi.org/10.1016/j.jmrt.2020.05.051.

[16] D.M. Stefanescu, G. Alonso, P. Larranaga, E. De La Fuente, R. Suarez, Reassessment of crystal growth theory of graphite in cast iron, Mater. Sci. Forum 925 (2018) 36—44. http://doi.org/10.4028/www.scientific.net/MSF.925.36.

[17] D.M. Stefanescu, R. Ruxanda, The liquid state and principles of solidification of cast iron, in: D.M. Stefanescu (Ed.), ASM Handb., 2017, pp. 46—58, https://doi.org/10.31399/asm.hb.v01a.a0006311.

[18] E. Moumeni, Solidification of Cast Iron -A Study on the Effect of Microalloy Elements on Cast Iron, 2013.

[19] H. Yasuda, Y. Yamamto, N. Nakatsuka, M. Yoshiya, T. Nagira, A. Sugiyama, I. Ohnaka, K. Uesugi, K. Umetani, Observation of solidification by using time-resolved X-ray imaging, in: S.L. Cockcroft, D.M. Maijer (Eds.), Proc. From 12th Int. Conf. Model. Cast. Welding, Adv. Solidif. Process., Minerals, Metals & Materials Society (TMS), 2009, pp. 245—252.

[20] R. Boeri, The Solidification of Ductile Cast Iron, 1989.

[21] K. Yamane, Y. Hideyiki, S. Akira, N. Tomoya, Y. Masato, U. Kentarou, U. Keiji, U. Chiaki, S. Akihiro, In-situ observation of solidification in hypereutectic Fe-3.8C-3.1Si alloys with Mg addition by time-resolved X-ray imaging, J. Japan Foundry Eng. Soc. 85 (2013) 760—770, https://doi.org/10.11279/jfes.85.760.

[22] H. Yasuda, A. Sugiyama, C. Kiattisaksri, K. Morishita, T. Nagira, M. Yoshiya, K. Uesugi, A. Takeuchi, X-ray imaging of formation and growth of spheroidal graphite in ductile cast iron, Mater. Sci. Forum 925 (2018) 104—109. http://doi.org/10.4028/www.scientific.net/MSF.925.104.

[23] J. Lacaze, U. De La Torre, J. Sertucha, A. Regordosa, Comparison of solidification kinetics of compacted and lamellar cast irons, IOP Conf. Ser. Mater. Sci. Eng. 861 (2020), https://doi.org/10.1088/1757-899X/861/1/012050.

[24] K. Chatcharit, A. Sugiyama, K. Morishita, T. Narumi, K. Kajiwara, H. Yasuda, Time evolution of solidification structure in ductile cast iron with hypereutectic compositions, Int. J. Met. 14 (2020) 794—801, https://doi.org/10.1007/s40962-020-00424-3.

[25] M.A. Azeem, M.K. Bjerre, R.C. Atwood, N. Tiedje, P.D. Lee, Synchrotron quantification of graphite nodule evolution during the solidification of cast iron, Acta Mater. 155 (2018) 393—401, https://doi.org/10.1016/j.actamat.2018.06.007.

[26] M. Drakopoulos, T. Connolley, C. Reinhard, R. Atwood, O. Magdysyuk, N. Vo, M. Hart, L. Connor, B. Humphreys, G. Howell, S. Davies, T. Hill, G. Wilkin, U. Pedersen, A. Foster, N. De Maio, M. Basham, F. Yuan, K. Wanelik, I12: the joint engineering, environment and processing (JEEP) beamline at Diamond light Source, J. Synchrotron Radiat. 22 (2015) 828—838, https://doi.org/10.1107/S1600577515003513.

[27] N. Wadeson, M. Basham, Savu: A Python-Based, MPI Framework for Simultaneous Processing of Multiple, N-Dimensional, Large Tomography Datasets, 2016. http://arxiv.org/abs/1610.08015.

[28] I. Asenjo, S. Mendez, J. Sertucha, P. Larranaga, R. Suarez, Experimental evidence for metallurgical modification associated to chunky graphite in heavy-section in ductile iron casting, Int. J. Met. 3 (2012) 35—42, https://doi.org/10.1007/BF03355476.

[29] M. König, Microstructure Formation during Solidification and Solid State Transformation in Compacted Graphite Iron, Jonkoping University, 2011.

[30] A. Kagawa, T. Okamoto, Partition of alloying elements in freezing cast irons and its effect on graphitization and nitrogen blowhole formation, in: S. Katz, C. Landefeld (Eds.), Proc. An Int. Symp. Foundry Process. Their Chem. Phys., New York, 1988, pp. 135—162. http://link.springer.com/10.1007/978-1-4613-1013-6.

[31] M.K. Bjerre, Mathias Karsten Bjerre PHD Thesis, 2017.

[32] S.N. Lekakh, X. Zhang, W. Tucker, H.K. Lee, T. Selly, J.D. Schiffbauer, Micro-CT quantitative evaluation of graphite nodules in SGI, Int. J. Met. 14 (2020) 318—327, https://doi.org/10.1007/s40962-019-00354-9.

[33] J. Qing, V.L. Richards, D.C. Van Aken, Examination of spheroidal graphite growth and austenite solidification in ductile iron, Metall. Mater. Trans. A

Phys. Metall. Mater. Sci. 47 (2016) 6197–6213, https://doi.org/10.1007/s11661-016-3783-1.

[34] D.M. Stefanescu, G. Alonso, P. Larrañaga, E. De La Fuente, R. Suarez, On the crystallization of graphite from liquid iron-carbon-silicon melts, Acta Mater. 107 (2016) 102–126, https://doi.org/10.1016/j.actamat.2016.01.047.

[35] H. Yasuda, A. Sugiyama, C. Kiattisaksri, K. Morishita, T. Nagira, M. Yoshiya, K. Uesugi, A. Takeuch, X-ray imaging of formation and growth of spheroidal graphite in ductile cast Iron, Mater. Sci. Forum 925 (2018) 104–109. http://doi.org/10.4028/www.scientific.net/MSF.925.104.

[36] E. Ghassemali, J.C. Hernando, D.M. Stefanescu, A. Dioszegi, A.E.W. Jarfors, J. Dluhoš, M. Petrenec, Revisiting the graphite nodule in ductile iron, Scripta Mater. 161 (2019) 66–69, https://doi.org/10.1016/j.scriptamat.2018.10.018.

[37] P. Zhu, R. Sha, Y. Li, Effect of twin/tilt on the growth of graphite, in: H. Fredriksson, M. Hillert (Eds.), Phys. Metall. Cast Iron. Proc. Third Int. Symp. Phys. Metall. Cast Iron, Stock. Sweden, August 29-31, 1984, pp. 3–11, https://doi.org/10.1557/PROC-34-3.

Peter D. Lee is Professor of Materials Science in the Department of Mechanical Engineering and Royal Academy of Engineering Chair in Emerging Technologies. His research focusses on x-ray imaging of materials at a microstructural level and then encapsulating the insights into computational simulations. Experimentally he develops nano-precision rigs that simulate the processing of materials on a synchrotron beamline, enabling us to see inside materials in 3D as they change in time. His group of 25 researchers is currently focusing on seeing into the heart of additive manufacturing using synchrotron imaging and diffraction coupled to other modalities.

Dr. Chaoling Xu received her Bachelor, MSc and PhD degrees in Material Science and Engineering from Chongqing University of Technology in 2011, Chongqing University in 2013, and the Technical University of Denmark (DTU) in 2017, respectively. After a short period at Linkoping University, she returned to DTU working as a Postdoctoral Researcher. Her activities focus on using advanced X-ray imaging techniques at both synchrotron facilities and laboratory instruments to study dynamic microstructure evolution of materials, including high-speed X-ray imaging of solidification of graphite evolution and diffraction contrast imaging to study the nucleation of recrystallization in deformed metals.

Tito Andriollo obtained MSc degrees in materials and in manufacturing engineering from the University of Padova and from the Technical University of Denmark (DTU), respectively, in 2013, and a PhD in mechanical engineering from DTU in 2017. After a short period at Eindhoven University of Technology, he returned to DTU where he currently works as tenure-track researcher. His activities focus on achieving mechanistic understanding of the processing-structure-properties relations for complex heterogeneous materials (primarily cast and additive manufactured metals) by exploiting combinations of computational and experimental techniques. Examples are micro-mechanics and computational homogenization, X-ray imaging, digital volume correlation and indentation-based methods.

Niels Skat Tiedje Associate Professor at the Department of Mechanical Engineering at the Technical University of Denmark. His research focusses solidification, microstructure and properties of metals in casting, welding and additive manufacturing. He has more than 20 years of experience with research in cast iron processing and microstructure analysis and modelling. More recently, he has taken on research in metallurgy and production of iron based metal powder for additive manufacturing with focus on recycled materials and optimisation of alloys for additive manufacturing.

Jesper Hattel (1965), obtained his M.Sc. in structural engineering in 1989 and his Ph.D. in mechanical engineering in 1993 both from DTU followed by a 2 year Marie Curie Fellowship in MAGMA, Aachen, Germany. Currently full professor in modelling of manufacturing processes at the Department of Mechanical Engineering, DTU where he also heads the Section for Manufacturing Engineering. Research interests are modelling of manufacturing processes like additive manufacturing, casting, joining and moulding. Applications vary from micro-scale to parts such as wind turbine blades. The area is highly cross-disciplinary involving CFD, Numerical Heat Transfer, Computational Metarials Science and Computational Solid Mechanics.

Tim Wigger has a degree in Mechanical Engineering (University of Applied Sciences Cologne), an MSc in Materials Science and Engineering (University of Siegen) and has worked as production analyst and engineering consultant in the manufacturing industry. He received his PhD in Mechanical Engineering from the University of Portsmouth and is currently a Research Fellow in the UCL Materials Structure and Manufacturing group based at Harwell Campus. He applies in situ high-speed synchrotron X-ray experiments to problems in alloy solidification kinetics, graphite morphology evolution in ductile cast iron and micromechanics of high-temperature high-strain rate steel forging processes.

Jean-Claude Grivel obtained a PhD in Condensed-Matter Physics at the Uniniversity of Geneva (Switzerland) in 1996. After postdoctoral positions at the Royal Institute of Technology (Stockholm/Sweden) and at Nordic Superconductor Technology A/S (Denmark), he joined the Risø National Laboratory, which was then merged with the Technical University of Denmark, where he is presently Associate Professor. His research activities are within materials engineering, with strong focus on metallurgy, superconduting wires and functional oxide thin films manufacture.

Mohammed Abdul Azeem My core research interest is in understanding microstructure-property correlations in metallic alloys, intermetallics and non-metals. This involves using various experimental techniques and modelling tools. I use advanced characterization techniques such as high energy X-rays, neutron and electron imaging and diffraction to capture, in real time, the effect of temperature, pressure and temperature-pressure on the micro, nano and sub-nano scale structure in materials. This is crucial for understanding and optimizing the processes used in production of all structural and functional materials. These world leading investigations are realized by extensive collaborations between research institutions, academia and industry.

Robert Atwood graduated from Engineering Science at University of Toronto followed by a Masters' degree in solidification in the Dept of Metallurgy and Materials Science. He obtained a PhD in Materials Science and Metallurgy at Imperial College London, studying the development of porosity defects during the solidification of metal castings via computational simulation. Subsequently he worked on the simulation and on characterization by imaging, applied to industrial materials, medical materials, and tissue/material interactions. He is currently a Senior Beamline Scientist at Diamond Light Source, bringing experiments in diverse fields to the I12-JEEP high-energy X-ray beamline, especially time-resolved in-situ process imaging.

Samuel Clark is a Beamline Scientist at the Advanced Photon Source at the Argonne National Laboratory where he works on the 32-id high speed imaging beamline. He principal field of research is in the *in situ* characterization of additive manufacturing processes. Prior to joining Argonne National Lab he was a Research Fellow at University College London under Professor Peter Lee.

Søren Fæster have 20 years of experience in materials science with focus on development and application of advanced characterization techniques. Laboratory responsible for the electron microscopes and X-ray tomography equipment at DTU Wind Energy. 2021—2024

WP leader on the characterization and modelling WP in the IFD funded project WeldCast. M.Sc. and PhD. Copenhagen University. Author of 76 int. publ. (46 journal papers and 30 conference papers), 1 patent.

Zhixuan Gong was graduated from UCL with a master degree of mechanical engineering in 2008. During the period of studying at UCL, he was awarded the Dean's list honor because of my outstanding academic performance. In 2019, he obtained a chance to keep studying in UCL as a doctoral student. The major topic of his research is to predict the size and density of defects inside the high pressure die casting product by establishing the appropriate simulation. Due to the personal reason, he withdrawn the research program in the May of 2020.